Applied Physics Letters

Large-depth-of-field optical-resolution colorectal photoacoustic endoscope

Cite as: Appl. Phys. Lett. **114**, 163703 (2019); https://doi.org/10.1063/1.5093789
Submitted: 25 February 2019 . Accepted: 13 April 2019 . Published Online: 26 April 2019

Xiaowan Li, Kedi Xiong, and Sihua Yang

Applied Physics Letters ARTICLE scitation.org/journal/apl

Large-depth-of-field optical-resolution colorectal photoacoustic endoscope

Cite as: Appl. Phys. Lett. **114**, 163703 (2019); doi: 10.1063/1.5093789
Submitted: 25 February 2019 · Accepted: 13 April 2019 ·
Published Online: 26 April 2019

Xiaowan Li,[1,2] Kedi Xiong,[1,2,a)] and Sihua Yang[1,2,b)]

AFFILIATIONS

[1]MOE Key Laboratory of Laser Life Science and Institute of Laser Life Science, South China Normal University, Guangzhou 510631, China
[2]College of Biophotonics, South China Normal University, Guangzhou 510631, China

[a)]xiongkd2012@163.com
[b)]yangsh@scnu.edu.cn

ABSTRACT

Defocus scanning, which causes a serious deterioration of the transverse resolution out of the focal zone, is a big obstacle to the application of optical-resolution photoacoustic (PA) endoscopy (OR-PAE) in imaging internal hollow organs. However, the current solution to generate an adjustable focal length is inapplicable for *in vivo* imaging due to the greatly increased scanning time. In this study, by applying an elongated focus lens that produces Bessel beams to the OR-PAE, we developed a large-depth-of-field optical-resolution PA endoscope with a depth of focus of ~8.6 mm in air, which can image targets at different depths without axial scanning, while maintaining a relatively constant transverse resolution. *Ex vivo* experimental results demonstrate the advantage of the endoscope to image biological tissues at different depths. Furthermore, an *in vivo* experiment presents three-dimensional vascular networks in the rabbit rectum, suggesting the potential of the endoscope for colorectal clinical applications.

Photoacoustic endoscopy (PAE) is a rapidly developing technique that embodies photoacoustic imaging (PAI) in a miniaturized probe to image internal organs.[1–5] As a label-free biomedical imaging modality, PAI is based on optical illumination and ultrasonic (US) detection.[6–10] According to whether the laser beam is focused, PAE can be categorized into two major types: acoustic-resolution (AR-) PAE and optical-resolution (OR-) PAE.[11] In AR-PAE, an area optical illumination is employed, and the spatial resolution is mainly determined by the intrinsic parameters of the US detector, such as the bandwidth, the numerical aperture, and the center frequency.[12–15] With this approach, the transverse resolution of images is generally greater than 100 μm. In contrast, OR-PAE utilizes a tightly focused beam to achieve a high transverse resolution of less than 100 μm at the expense of imaging depth, which is smaller than 1 mm due to the light scattering in biological tissues;[16–20] whereas the axial resolution is still determined by the time-resolved US detection.[12,21] Therefore, compared to AR-PAE, OR-PAE has greater vasculature resolving ability owing to its higher transverse resolution.

Several groups have reported optical-resolution PA probes to image blood vessels in internal organs. However, most of them utilize a graded-index lens to focus light,[22–25] thus generating a fixed depth of focus (DOF) of much less than 1 mm, which generally causes defocus scanning when internal hollow organs are imaged due to the difficulty in ensuring that all targets at different positions are within such a short DOF. Since the transverse resolution is seriously degraded out of the focal zone, an autofocusing OR-PAE was developed in our previous work to address the issue of defocus scanning.[26] Nevertheless, changing the focal length requires additional scanning time and complex data processing, which is unsuitable for real-time colorectal imaging.

Recently, many methods have been introduced to extend the DOF in optical imaging fields, such as spatial multiplexing,[27] layer-by-layer frequency domain imaging,[28] deformable mirror,[29] spatial light modulator,[30] and synthetic Bessel light needle.[31] Although the proposed methods are effective for DOF extension, those complicated devices are inapplicable for endoscopic systems. Here, by utilizing an elongated focus (EF) lens to generate Bessel beams, we developed a large depth-of-field colorectal PA endoscope, which achieves relatively constant transverse resolution at different depths without axial scanning. Despite the fact that a conical lens can also generate Bessel beams, it has difficulty in fabricating an ideal conical surface, and the manufacturing errors can distort the Bessel beams.[32–36] Nevertheless, by employing computer-generated lithographic masks and etching

technology to produce a continuous microstructure relief pattern, the diffractive EF lens alters the phase of incident collimated beams to create Bessel beams with high precision and high efficiency.

Figure 1(a) shows the schematic of the entire PAE system. A trigger module provides a synchronous trigger for a pulsed laser (527 nm, 7 ns pulse width) and a data acquisition system. Laser pulses are coupled to a single-mode fiber and focused by a lens group, and eventually, the focused laser beams are transmitted to the target tissue after passing through the scanning head. Inside the probe, a stepper motor and a linear motor are actuated by an external motor driver to control the scanning head for rotation and linear motion. The PA signals detected by the scanning head are amplified to ∼50 dB by an amplifier (LNA-650, RF Bay) and then digitally recorded using a data acquisition card (100 MHz, M3i.4110, Spectrum). Finally, the reconstructed images are displayed on a computer. Figure 1(b) shows a photo of the probe. To encapsulate the probe, a biocompatible acrylonitrile butadiene styrene plastic tube (8 mm outer diameter, 12 cm length) and a transparent medical-grade polystyrene coupling window (500 μm thickness, ∼2 cm length) were fabricated. An iron block is embedded in the bottom of the housing; hence, the probe can be flexibly attached to or removed from the mechanical arm by switching on or off the magnetic base.

Figure 1(c) presents a schematic to illustrate the built-in three-dimensional (3D) scanning structure of the probe. Inside the housing, a rotating shaft is supported by a sliding plastic case (SPC) through a custom-built sliding bearing, which ensures the smooth rotation of the rotating shaft. The optical focusing unit is encapsulated by a lens holder, which is fixed to the SPC and coaxial with the rotating shaft. The scanning head is sustained by the rotating shaft to achieve

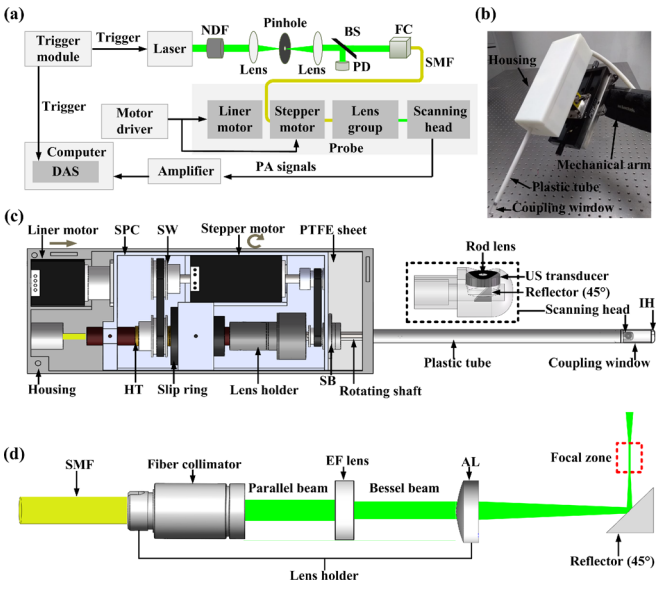

FIG. 1. (a) Block diagram of the PAE system. NDF, neutral density filter; BS, beam splitter; PD, photodiode; FC, fiber collimator; SMF, single-mode fiber; and DAS, data acquisition system. (b) Photo of the probe and the peripheral fixed platform. (c) Schematic of the detailed structure of the probe. SPC, sliding plastic case; SW, synchronizing wheel; PTFE, polytetrafluoroethylene; HT, hollow tube; SB, sliding bearing; and IH, injection hole. (d) Schematic of the configuration of the optical components. AL, aspherical lens.

mechanical scanning. The key component of the scanning head is a customized ring-shaped US transducer (unfocused, 15 MHz, 71% bandwidth) with an outer diameter of 5 mm and an inner diameter of 2.5 mm, which is used to detect PA signals. A rod lens (2.5 mm diameter) located at the center of the US transducer was fabricated to transmit light reflected by a reflector (45°) and seal the hole. Hence, the optical illumination and the acoustic detection can be realized coaxially to optimize the sensitivity. The signal wire in the scanning head passes through the groove of the 14 cm long rotating shaft and connects to the slip ring. A hollow tube was fabricated to act as a rotating shaft of the slip ring; hence, when actuated by a stepper motor and four synchronous wheels, the rotating shaft and the slip ring rotate synchronously. To achieve 3D imaging, a linear motor was employed to move the SPC back and forth. Limited by the length of the coupling window, the maximum longitudinal length for a C-scan is ∼1 cm. An O-ring at the distal end of the rotating shaft was exploited to seal the gap between the rotating shaft and the plastic tube. Hence, acoustic coupling inside the probe can be realized by injecting water into the probe through an injection hole (∼1 mm diameter) in the coupling window. However, as the scanning head moves forward, water flows out of the injection hole, and thus the scanning head needs to be pulled back after a C-scan for another water injection. Moreover, a 0.5 mm thick polytetrafluoroethylene (PTFE) sheet was placed under the SPC; thus, the linear motion can be carried out smoothly. When a C-scan is performed, the plastic tube and the housing remain stationary.

Figure 1(d) illustrates the optical assembly in the probe. Laser pulses exited from a single-mode fiber are collimated by a customized fiber collimator composed of an aspherical lens (352610-A, Olympus) into parallel beams (∼4 mm diameter). Then, the collimated beams pass through an 11-mm diameter EF lens (EF-023-IYA, HOLO/OR) with a focal length of ∼152 mm to generate Bessel beams, which are focused by an aspherical lens (#48–185, Edmund) and sent to the target through the reflector inside the scanning head. The DOF is proportional to the focal length of the focusing lens, and inversely proportional to the collimated beam diameter. Additionally, the increase in the wavelength or refractive index of the medium also extends the DOF, but at the cost of increasing the spot size.

Before assembling the lens group into the probe, we quantified the performance of the output beam. Figure 2(a) shows the simulated optical intensity map of the focal zone. In the simulation, the beam quality M^2 and the refractive index n are set to 1. Considering that the coupling medium we used for PA imaging is water, and assuming that laser beams that exited from the rod lens are in the range of 135 mm to 170 mm along the optical axis, another simulation was performed by changing n to 1.33 in this range [Fig. 2(b)]. In Figs. 2(a) and 2(b), the distance between the two white lines is the DOF, which is defined as the range for which intensity (Y = 0) is greater than 1/2 of the maximum value; the two red lines depict the theoretically spot size at full width at half maximum (FWHM). Hence, when the coupling medium is air (n = 1) and water, the DOF is 8.6 mm and 9.8 mm, respectively. Furthermore, in Fig. 2(a), the beam size within the DOF ranges from 17.5 μm to 36.8 μm. However, in Fig. 2(b), the spot size in the DOF varies from 22.3 μm to 44.7 μm.

To validate the simulation results, an experimental measurement of the beam size was implemented. After the optical fiber was connected to the fiber collimator, the lens holder was mounted on a

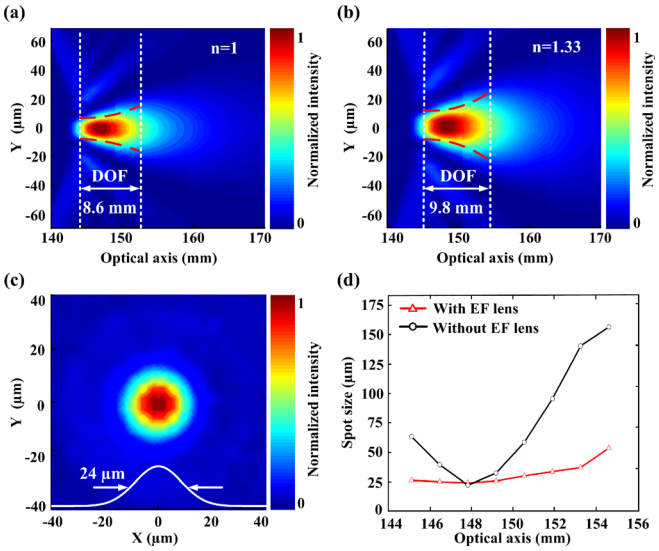

FIG. 2. (a) and (b) Simulated transmission (i.e., one-way) light intensity maps of the focal zone when the refractive index n of the coupling medium (in a range from 135 mm to 170 mm along the optical axis) is 1 and 1.33, respectively; while in the rest of the region both have a refractive index of 1. The distance between the two white lines is the DOF, and the two red lines depict the theoretically calculated spot size at full width at half maximum (FWHM). (c) Experimentally measured minimum laser beam intensity profile in the focal zone (n = 1). (d) Experimentally measured variation of the spot size along the optical axis with and without an EF lens.

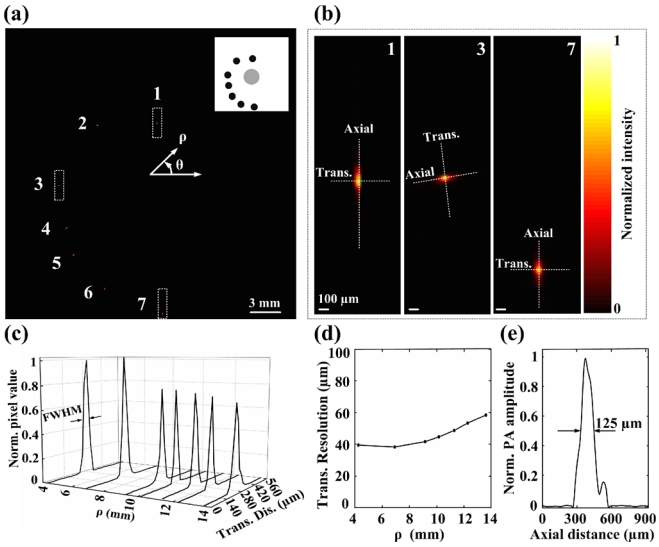

FIG. 3. (a) PA B-scan image of seven carbon fibers with a diameter of 7 μm at different depths. (b) The magnified images of dashed rectangles in (a). (c) Transverse point spread functions (PSFs) of the seven carbon fibers in (a). (d) FWHM of the transverse PSFs extracted from (c). (e) Axial resolution of the carbon fiber at position 1 in (a).

one-dimensional translation stage with an adjustable range of 50 mm. A beam profiler was aligned with the lens group to ensure that the laser beam is perpendicularly illuminated on the beam profiler. According to the results in Fig. 2(a), after finding the smallest beam size at a distance of ~147.8 mm, we recorded the spot size within the range of 9.45 mm at a 1.35 mm step size. As shown in Fig. 2(c), the minimum FWHM-based beam diameter is ~24 μm, which is larger than the simulation result of 17.5 μm; the discrepancy is mainly due to the worse beam quality than the theoretical value. Figure 2(d) illustrates the variation of the spot size along the optical axis with and without the EF lens. When the EF lens is used, the spot size changes by ~21 μm within 8.6 mm, which is basically consistent with the theoretical simulation results [Fig. 2(a)]. Nevertheless, without the EF lens, the spot size varies by ~126 μm in the same range, indicating the significant advantage of the EF lens. Consequently, a focal length of ~147.8 mm and a DOF of ~8.6 mm were recorded as parameters of the lens group in air. When the coupling medium is water, the focal length and the DOF increase by about 1.5 mm and 1.2 mm, respectively. Additionally, based on the discrepancy in the spot size (n = 1) between simulation and experiment, it is speculated that the actual spot size is within a range of ~28.8 μm to ~51.2 μm when the coupling medium is water.

Seven carbon fibers (~7 μm thickness) were utilized as targets to evaluate the spatial resolution of the endoscope. In the phantom, carbon fibers were imaged from a 4.32 mm to 13.8 mm distance in water medium. Based on the results in Fig. 2, we adjusted the distance between the lens holder and the reflector to cover all targets in the DOF. Figure 3(a) shows a PA B-scan image of the optical phantom. Figure 3(b) presents enlarged views of the dashed boxes in (a). Figure 3(c) illustrates the transverse point spread functions (PSFs) for the carbon fibers located at seven different depths [Fig. 3(a)]. It can be concluded from Figure 3(c) that the optical intensity at 13.8 mm decreases by 48% compared with that at 7.12 mm. In Fig. 3(d), according to the FWHM of the PSFs extracted from Fig. 3(c), the optimal transverse resolution (~40.18 μm) is around at the imaging depth of 7.12 mm. In the range of 9.48 mm, the transverse resolution is reduced by ~24 μm. The experimental transverse resolution is lower than that predicted in Fig. 2. The discrepancy may be mainly due to the imperfections in the coupling window. Figure 3(e) shows the PA A-line Hilbert-transformed signal at 7.12 mm. Based on the FWHM of the PSF, the axial resolution is 125 μm, which is basically consistent with the theoretical axial resolution[13] (117 μm).

To illustrate the imaging feasibility of the endoscope on biological tissues at different depths, *ex vivo* imaging of an excised small intestine of a pig was performed. As shown in Fig. 4(a), the small intestine was placed on the outside surface of a noncircular hollow agar gel, which is filled with water, then the probe was inserted into the hole of the agar gel. Moreover, a contrast experiment was conducted by taking out the EF lens. Figures 4(b) and 4(c) show the representative PA B-scan image with and without the EF lens. Figures 4(d) and 4(e) show enlarged views of the dashed boxes in Figs. 4(b) and 4(c), respectively. As shown in Fig. 4(d), both subimages located in different areas clearly provided the distribution of the vasculature. However, without the EF lens, the blood vessels in the defocus area were not clearly distinguished owing to the deteriorated transverse resolution. Besides, due to the light scattering in agar and the loss of blood in the excised small intensity, only partial large blood vessels can be imaged.

To further demonstrate the full vasculature resolving capability of the endoscope, we imaged the rectum of a New Zealand white rabbit (~2.5 kg, female). Before the experiment, the rabbit was fasted

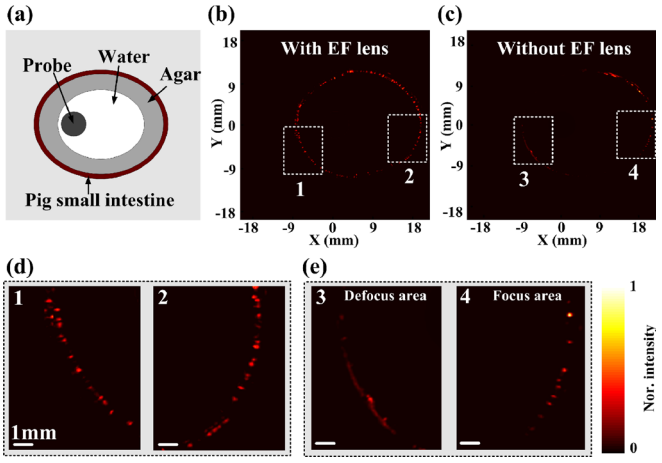

FIG. 4. (a) Schematic of an excised pig small intestine imaging experiment. (b) PA B-scan image with the EF lens. (c) PA B-scan image without the EF lens. (d) and (e) Representative magnified B-scan images in (b) and (c). The two subimages 1 and 2 represent the nearest and the farthest areas in (b), respectively. The two subimages 3 and 4 represent the areas of defocus and focus in (c), respectively.

for ∼12 h to make its rectum as empty as possible. Afterwards, the rabbit was anesthetized by injecting 1 g/kg urethane intravenously and placed on a tilted thermostatic stage (∼10°) in a supine position. Once the rabbit was properly fixed, we gave it a saline enema and filled its rectum with clear water for acoustic coupling. During the imaging process, anesthesia was maintained with 1.5% to 3% isoflurane through a mask. Then, the probe was inserted into the rectum and fixed on the mechanical arm. In the experiment, the laser pulse energy is 2 μJ at an 8 kHz repetition rate, which yields an optical fluence of 12.5 mJ/cm^2 (62.5% of the ANSI safety limit[37]). To achieve a C-scan, we recorded images with a 2 Hz B-scan frame rate when the linear motor actuated the scanning head to move at a speed of 40 μm/s. All procedures in the experiment were approved by the South China Normal University.

Figure 5 presents the *in vivo* imaging results. Figure 5(a) shows a volume rendered image from the rabbit rectum. The image was processed from 400 B-scan slices over a scanning time of ∼3.3 min; thus, it covers an 8-mm longitudinal length. Figure 5(b) shows a subimage of the selected region in Fig. 5(a), clearly presenting the blood vessels in the rectum and the adjacent mesentery. As shown in the radial-maximum amplitude projection (RMAP) image [Fig. 5(c)], in the later stages of imaging, the imaging quality decreases due to the effect of air bubbles. Figures 5(d) and 5(e) present B-scan images selected from position I and position II in Fig. 5(c), respectively. Although the rectal diameters of the two positions differ by ∼1 mm, it can be seen from the subimages 1 and 2 that both present blood vessels as small as ∼50 μm in diameter, so there is no significant deterioration in transverse resolution due to the long DOF.

In summary, we developed a PA endoscope with ∼8.6 mm DOF in air and demonstrated its imaging capability through *ex vivo* and *in vivo* animal experiments. The transverse resolution of the endoscope in water medium varies from 41.8 μm to 62 μm in a range of 9.48 mm. Compared with an autofocusing endoscope, the merits of the large depth-of-field and the built-in scanning structure make the endoscope more suitable for clinical 3D imaging of the colorectum.

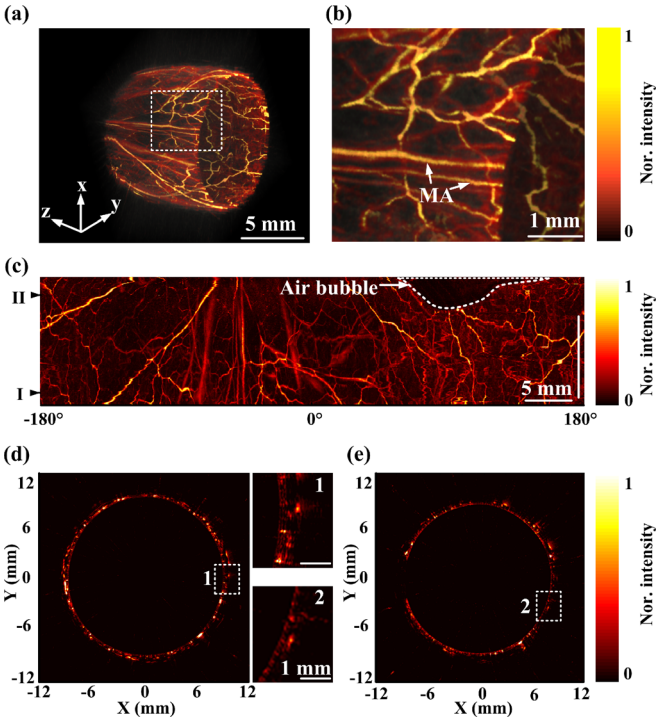

FIG. 5. (a) *In vivo* PA image of a rabbit rectum. (b) The magnified image of the dashed rectangle in (a). MA, mesenteric artery. (c) The radial-maximum amplitude projection (RMAP) image of (a). (d) and (e) Representative B-scan images selected from position I and position II marked in (c), respectively. The rectal diameters of the two positions differ by ∼1 mm. The two typical subimages 1 and 2 are magnified images of dashed rectangles in (d) and (e), respectively.

Nevertheless, the length of the plastic tube, which is limited by the focal length of the lens group, is only 12 mm. In the future, the effective length of the probe can be increased by employing a smaller lens group that can be mounted inside the scanning head. Furthermore, the convex surface of the coupling window causes geometric acoustic aberration, thus decreasing the sensitivity of the US transducer. Replacing the rigid coupling window with a transparent elastic membrane will improve the image quality and eliminate the attenuation of ultrasound and light. As the endoscope presents PA images with 3D vasculature information, it has potential for imaging colorectal tumors and thereby provide clinicians with appropriate treatment protocols for colorectal diseases.

This research was supported by the National Natural Science Foundation of China (Nos. 61822505; 11774101; 61627827; 81630046; and 11604105), the Science and Technology Planning Project of Guangdong Province, China (No. 2015B020233016), and the Science and Technology Youth Talent for Special Program of Guangdong, China (No. 2015TQ01X882).

REFERENCES

[1]J.-M. Yang, K. Maslov, H.-C. Yang, Q. Zhou, K. K. Shung, and L. V. Wang, Opt. Lett. **34**, 1591 (2009).
[2]J.-M. Yang, R. Chen, C. Favazza, J. Yao, C. Li, Z. Hu, Q. Zhou, K. K. Shung, and L. V. Wang, Opt. Express **20**, 23946 (2012).

[3]Y. Yuan, S. Yang, and D. Xing, Opt. Lett. **35**, 2266 (2010).
[4]D. Cai, G. Li, D. Xia, Z. Li, Z. Guo, and S.-L. Chen, Opt. Express **25**, 20163 (2017).
[5]H. He, A. Buehler, and V. Ntziachristos, Opt. Lett. **40**, 4667 (2015).
[6]L. V. Wang and S. Hu, Science **335**, 1458 (2012).
[7]J. Tick, A. Pulkkinen, and T. Tarvainen, J. Acoust. Soc. Am. **139**, 1951 (2016).
[8]J. Y. Kim, C. Lee, K. Park, G. Lim, and C. Kim, Sci. Rep. **5**, 7932 (2015).
[9]G. Li, F. Gao, Y. Guo, X. Feng, and Y. Zheng, Appl. Phys. Lett. **109**, 013701 (2016).
[10]L. Xiang, B. Wang, L. Ji, and H. Jiang, Sci. Rep. **3**, 1113 (2013).
[11]P. Beard, Interface Focus **1**, 602 (2011).
[12]S. Mallidi, G. P. Luke, and S. Emelianov, Trends Biotechnol. **29**, 213 (2011).
[13]C. Zhang, K. Maslov, J. Yao, and L. V. Wang, J. Biomed. Opt. **17**, 116016 (2012).
[14]O. Simandoux, N. Stasio, J. Gateau, J.-P. Huignard, C. Moser, D. Psaltis, and E. Bossy, Appl. Phys. Lett. **106**, 094102 (2015).
[15]F. Kong, Y. C. Chen, H. O. Lloyd, R. H. Silverman, H. H. Kim, J. M. Can-nata, and K. K. Shung, Appl. Phys. Lett. **94**, 033902 (2009).
[16]P. Hajireza, T. Harrison, A. Forbrich, and R. Zemp, J. Biomed. Opt. **18**, 090502 (2013).
[17]I. N. Papadopoulos, O. Simandoux, S. Farahi, J. P. Huignard, E. Bossy, D. Psaltis, and C. Moser, Appl. Phys. Lett. **102**, 211106 (2013).
[18]P. Hajireza, W. Shi, and R. J. Zemp, Opt. Lett. **36**, 4107 (2011).
[19]W. Shi, P. Hajireza, P. Shao, A. Forbrich, and R. J. Zemp, Opt. Express **19**, 17144 (2011).
[20]H. Guo, C. Song, H. Xie, and L. Xi, Opt. Lett. **42**, 4615 (2017).
[21]Y. Li, R. Lin, C. Liu, J. Chen, H. Liu, R. Zheng, X. Gong, and L. Song, J. Biophotonics **11**, e201800034 (2018).
[22]B. Dong, S. Chen, Z. Zhang, C. Sun, and H. F. Zhang, Opt. Lett. **39**, 4372 (2014).
[23]H. He, G. Wissmeyer, S. V. Ovsepian, A. Buehler, and V. Ntziachristos, Opt. Lett. **41**, 2708 (2016).
[24]P. Hajireza, W. Shi, and R. Zemp, Laser Phys. Lett. **10**, 055603 (2013).
[25]J. M. Yang, C. Li, R. Chen, B. Rao, J. Yao, C. H. Yeh, A. Danielli, K. Maslov, Q. Zhou, K. K. Shung, and L. V. Wang, Biomed. Opt. Express **6**, 918 (2015).
[26]K. Xiong, S. Yang, X. Li, and D. Xing, Opt. Lett. **43**, 1846 (2018).
[27]K.-C. Kwon, M.-U. Erdenebat, M. A. Alam, Y.-T. Lim, K. G. Kim, and N. Kim, Opt. Express **24**, 2072 (2016).
[28]J. Yang, L. Gong, X. Xu, P. Hai, Y. Shen, Y. Suzuki, and L. V. Wang, Nat. Commun. **8**, 780 (2017).
[29]W. J. Shain, N. A. Vickers, B. B. Goldberg, T. Bifano, and J. Mertz, Opt. Lett. **42**, 995 (2017).
[30]W. Song, Y. Wu, Y. Gao, T. Chen, W. Zheng, H. Fang, L. Song, and X. Yuan, Appl. Phys. Lett. **113**, 163502 (2018).
[31]J. Yang, L. Gong, Y. Shen, and L. V. Wang, Appl. Phys. Lett. **113**, 181104 (2018).
[32]J. Dudutis, P. GeČys, and G. RaČiukaitis, Opt. Express **24**, 28433 (2016).
[33]J. Dudutis, R. Stonys, G. Račiukaitis, and P. Gečys, Opt. Express **26**, 3627 (2018).
[34]P. Wu, C. Sui, and W. Huang, Photonics Res. **2**, 82 (2014).
[35]S. Akturk, B. Zhou, B. Pasquiou, M. Franco, and A. Mysyrowicz, Opt. Commun. **281**, 4240 (2008).
[36]X. Zeng and F. Wu, Opt. Eng. **47**, 083401 (2008).
[37]Laser Institute of America, *American National Standard for Safe Use of Lasers ANSI Z136.1-2014* (American National Standards Institute, Inc., 2014).